ADVANCED ELECTRONIC MATERIALS Open Access
www.advelectronicmat.de

Temperature-Dependent Dynamics of Charge Carriers in Tellurium Hyperdoped Silicon

*KM Ashikur Rahman, Mohd Saif Shaikh, Qianao Yue, S. Senali Dissanayake, Mao Wang, Shengqiang Zhou, and Meng-Ju Sher**

Tellurium-hyperdoped silicon (Si:Te) shows significant promise as an intermediate band material candidate for highly efficient solar cells and photodetectors. Time-resolved THz spectroscopy (TRTS) is used to study the excited carrier dynamics of Si hyperdoped with 0.5, 1, and 2%. The two photoexcitation wavelengths enable us to understand the temperature-dependent carrier transport in the hyperdoped region in comparison with the Si region. Temperature significantly influences the magnitude of transient conductivity and decay time when photoexcited by light with a wavelength of 400 nm. Due to the differential mobilities in the Si and hyperdoped regions, such dependence is absent under 266-nm excitation. Consistent with the literature, the charge-carrier lifetime decreases with increasing dopant concentration. It is found that the photoconductivity becomes less temperature-dependent as the dopant concentration increases. In the literature, the photodetection range of Si:Te extends to a wavelength of 5.0 μm at a temperature of 20 K. The simulation shows that carrier diffusion, driven by concentration gradients, is strongly temperature dependent and impacts transient photoconductivity decay curves. The simulation also revealed that, in the hyperdoped regions, the carrier recombination rate remains independent of temperature.

1. Introduction

Optoelectronic devices based on Si have photosensitivity limited by the band gap energy of Si (1.1 eV, which corresponds to light with a wavelength of 1.12 μm). Hyperdoping Si could radically transform its light absorption properties, allowing it to absorb light across a wide range of wavelengths.[1,2] This could enable new and exciting opportunities for Si-based IR optoelectronics.[3–6] One of the primary challenges in hyperdoped Si-based optoelectronics is low quantum efficiency.[7–10] A recent breakthrough in hyperdoped-Si-based photodetectors extended the detection range to 5 μm at cryogenic temperatures.[11,12] In another study, integrating graphene with Si:Te significantly enhanced the photodetector performance, achieving an ultrahigh photogain of 10^9 a at room temperature and 10^{12} at 80 K using photoexcitation at 1.55 μm.[13] Additionally, at room temperature, the detector demonstrated a high gain at 2.7 μm surpassing traditional InGaAs photodetectors that are restricted to wavelengths below 1.7 μm.[13] However, very little is known about charge-carrier trapping and transport in hyperdoped systems at different temperatures. Understanding the fundamental charge carrier dynamics and recombination processes in these materials is crucial for the development of optoelectronic devices. In this study, we investigate the influence of temperature and doping concentration on carrier transport and lifetime in Si:Te.

Deep-level dopants introduce energy states within the band gap of Si that are neither close to the conduction nor valence bands and change the optical and electronic properties of the material. The process of hyperdoping significantly increases the density of these deep-level states[7,14–16] and enables the absorption of photons with energies lower than the band gap energy.[15,17,18] Literature shows that chalcogen-hyperdoped Si exhibits light absorption extending up to 8 μm.[19,20] However, these deep levels also act as recombination centers, which can lead to faster carrier recombination and consequently, shorter carrier lifetimes.[15] The foreign atoms can also act as scattering centers for charge carriers, which lead to a reduction in the mobility of charge carriers. For the development of effective photovoltaic devices using hyperdoped Si with deep-level dopants, the primary challenge is to strike a balance: significantly enhancing the absorption of sub-bandgap light while carefully minimizing their detrimental effects on both the lifetime and mobility of the charge carriers.[21–23]

In our work hyperdoping is achieved by ion implantation followed by pulsed laser melting (PLM).[4,21] The process begins

K. A. Rahman, Q. Yue, S. S. Dissanayake, M.-J. Sher
Wesleyan University
Middletown, Connecticut 06459, USA
E-mail: msher@wesleyan.edu
M. S. Shaikh, M. Wang, S. Zhou
Helmholtz-Zentrum Dresden-Rossendorf
Institute of Ion Beam Physics and Materials Research
Bautzner Landstasse 400, 01328 Dresden, Germany

The ORCID identification number(s) for the author(s) of this article can be found under https://doi.org/10.1002/aelm.202400417

DOI: 10.1002/aelm.202400417

with bombardment of a Si substrate with high-energy dopant ions in a vacuum environment. This ion implantation step introduces dopant atoms into the Si lattice at controlled depths and concentrations. To achieve the high concentration required, a high implantation dose damages and amorphizes the Si lattice. Next, PLM is performed to restore crystallinity. In this step, the implanted Si surface is exposed to an intense ns-laser pulse. The pulse energy is sufficient to melt the Si surface to a depth beyond the ion implantation depth so that the underlying crystalline solid can act as a template for crystal regrowth. As the material rapidly cools and recrystallizes, the dopant atoms are locked into the host lattice at concentrations far exceeding the equilibrium solubility limits.[2,24,25] This method offers several advantages. First, rapid melting and solidification prevent the dopant atoms from forming clusters or precipitates, resulting in a single-crystalline and uniform material. Second, PLM allows for precise control over the depth and concentration of the dopant layer, which is essential for tailoring the optoelectronic properties of the material. Finally, the high dopant concentrations achievable through this method can significantly alter the electrical and optical properties of Si, allowing the creation of novel semiconductor devices with enhanced or entirely new functionalities.[26–28]

Heavy chalcogens, when used as dopants in Si, provide better structural stability compared to transition metals due to their lower diffusion velocities. This property prevents them from migrating to the surface and causing cellular breakdown during the PLM process. It is demonstrated that Te can be incorporated at high concentrations without exhibiting cellular breakdown and achieved n-type doping with a carrier density as high as 8.3×10^{20} cm^{-3}.[1,11,17,18] Te is more thermally stable than sulfur (S) or selenium (Se) due to lower diffusivity and higher activation energy.[29] Te maintains strong sub-bandgap light absorption capabilities even after thermal annealing at 400°C for 10 min. In contrast, sulfur (S) and selenium (Se) hyperdoped Si lose significant sub-bandgap light absorptions under the same conditions.[24,30] Specifically, Te introduces deep-donor states into Si at energy levels of 0.20 and 0.41 eV below the conduction band (CB) edge.[12,31,32] These two states merge at high concentrations into a quasi-continuous intermediate band, significantly altering the band structure to facilitate enhanced sub-bandgap absorption.[12,16] As a result, Si:Te-based photodetectors enhance the photoresponse in the mid-infrared region, operable at room temperature, while being compatible with CMOS technology.

For IR photodetectors or solar cells, the device efficiencies depend crucially on fundamental material properties, such as carrier mobility (μ) and lifetime (τ).[23] How easily free carriers move within the material depends on μ, and μ depends on factors such as lattice vibration, impurity type, and concentration, and whether these impurities are substitutional or interstitial. In pure or lightly doped Si, mobility is mainly affected by phonon scattering.[33] With increasing temperature, the lattice vibration increases, leading to more phonon scattering and decreased mobility. In hyperdoped Si, impurity scattering is dominant because of the high dopant concentration. The carrier mobility in hyperdoped Si is reduced by one to two orders of magnitude compared with that in lightly doped Si. However, above a certain dopant concentration, the carrier mobility reaches a steady value, independent of the carrier concentration in the ultrahigh doping regime.[34]

The duration for which charge carriers retain excess energy and contribute to photosensing or power generation is determined by τ. The carrier lifetime is influenced by the density of defects or trap states (N_{trap}), electron capture cross-section of electrons encountering these traps (σ), and thermal velocity of charge carriers ($v_{thermal}$). Assuming that trap state densities are high and detrapping probabilities are low, the recombination rate, or the inverse of τ, is described by the following relationship:[35]

$$\frac{1}{\tau} = N_{\text{trap}} \cdot \sigma \cdot v_{\text{thermal}} \tag{1}$$

How τ changes with temperature depends on how σ and v_{thermal} change with temperature, and we briefly review different scenarios below.

First, if σ is temperature independent, then the temperature dependence of the carrier lifetime stems from v_{thermal}. The thermal velocity is given by the expression $v_{\text{thermal}} = \sqrt{\frac{3k_BT}{m^*}}$ where k is the Boltzmann constant, T is the temperature, and m^* is the effective mass of the carrier. As the temperature decreases, v_{thermal} of the carriers also decreases, leading to a reduced likelihood of electron–hole recombination. Consequently, the carrier lifetime increases as the temperature falls, following the relation $\tau \propto \frac{1}{\sqrt{T}}$. In 1992, A. Schenk presented a model that aligns with this understanding, predicting the relationship between temperature and Shockley–Read–Hall recombination rates.[36] Experimentally, carrier lifetimes that increase with decreasing temperature with a square root relation have been observed in gold-doped silicon.[36]

On the other hand, depending on the nature of trap states, σ can either increase or decrease with the temperature. For instance, for semiconductor materials, such as GaAs and GaP, σ is dominated by multiphonon emission.[37] It exhibits a temperature dependence that is thermally activated, represented by the equation $\sigma = \sigma_\infty \cdot e^{-\frac{E_0}{kT}}$, leading to an increased capture cross-section σ at higher temperatures. This study further elaborates on the role of lattice vibrations in altering the potential well depth, which directly influences the probability of carrier capture. It provides experimental evidence supporting significant lattice relaxations at high temperatures, which are pivotal in explaining the large electron and hole capture cross sections observed.

In the literature, a few more examples have shown different temperature-dependent trends associated with the reduction of σ with increasing temperature. Masaya et al., found that in lightly doped Si wafers, σ decreased with increasing temperature.[38] Similarly, Padual et al., observed a trend in which σ decreased with increasing temperature in molybdenum-doped Si across a broad temperature range.[39] Rein et al., explored this behavior in molybdenum-doped Si and established a relationship between σ and temperature as $\sigma \propto \frac{1}{\sqrt{T}}$.[40]

In this study, we aim to explore the effects of temperature changes on the carrier lifetime of Si:Te. Our focus is to understand how temperature influences the various properties of Si:Te and how these changes translate into variations in carrier lifetime. We employ -TRTS- to understand the dynamics of Si:Te.[41] TRTS is a non-contact method that is ideal for studying potential

materials without any electric contact. The optical pump pulse excites the carriers within the material, and the subsequent THz probe pulse measures the change in the transient conductivity of the material. The time delay between the pump and probe provides a temporal resolution on the order of picoseconds, offering insights into rapid carrier dynamics. Photoexcitation at 400 nm allows us to probe the dynamics both near the material surface and deeper within. Furthermore, by utilizing 266 nm excitation, we can focus on the behavior of electrons specifically within the hyperdoped region. Our temperature-dependent studies range from 100 to 310 K, ensuring a comprehensive understanding of the material across a spectrum of conditions.

The samples used in this study are Si:Te with dopant concentrations of 0.5, 1, and 2 atomic%. The samples were fabricated under the same conditions described in ref. [12]. Te dopants primarily substitute the Si lattice positions, resulting in materials with strong sub-bandgap absorption that varies with dopant concentration,[12] while the above-bandgap light absorption is unchanged.[1] The dopant distribution is uniform to a depth of 100 nm. Although the exact energy levels of the dopants are not known, literature indicates that at dilute concentrations, Te acts as a double donor with energy levels of 0.2 and 0.41 eV below the conduction band. At higher concentrations, these dopant states merge into an impurity band.[12,16,31,32] Our previous publications[11,12] demonstrate that photodiodes made from these samples exhibit extended infrared photoconductivity of up to 4 μm at room temperature and 5 μm at cryogenic temperatures.

2. Simulation

We used a 1D diffusion and recombination equation to simulate the decay dynamics of Si:Te. The equation is given by:

$$\frac{\partial n_e(x,t)}{\partial t} = D(x)\frac{\partial^2 n_e(x,t)}{\partial x^2} - \frac{n_e(x,t)}{\tau(x)} \tag{2}$$

In this equation, $n_e(x, t)$ represents the concentration of photoexcited carriers (e.g., electrons) at any given position x and time t. The term $D(x)$ denotes the diffusion coefficient, which is linked to $\mu(x)$ through the Einstein relation $D = \mu(x)k_bT$, where k_b is Boltzmann's constant, and T denotes temperature. The carrier lifetime, $\tau(x)$, and its inverse, the recombination rate, are described by $\frac{1}{\tau} = n_{Te}(x)\sigma v_{\text{thermal}}$, where $n_{Te}(x)$ indicates the Te concentration at depth x. The model distinguishes between two distinct regions: the hyperdoped region from the surface $x = 0$ to $x = 100$ nm and the substrate region from $x = 100$ nm to $x = 3000$ nm. $D(x)$ is spatially dependent because μ in the hyperdoped region is lower than that in the substrate, and $\tau(x)$ is spatially dependent because we assume that the recombination centers are Te dopants so $\tau(x)$ is small in the hyperdoped region. In the substrate region, where the dopant concentration is significantly lower than that in the hyperdoped region, σ becomes zero, and carrier dynamics are primarily governed by diffusion. In the following paragraphs, we discuss how we set up the simulation parameters in the hyperdoped and substrate regions and their temperature dependencies.

For μ in the hyperdoped region, a range of values was examined. ref. [16] reported the Hall mobility of Si:Te with different concentrations at 2 and 310 K. The study suggests that μ is weakly dependent on concentration and temperature. We tested values within the reported range with and without temperature dependence.

For τ in the hyperdoped region, the recombination rate depends on the concentration of Te dopants. The dopant distribution in the hyperdoped region was obtained directly from ref. [12], which is constant in the hyperdoped region, and decreases to zero in the substrate region. As discussed in the introduction, the dependence of σ on temperature varies depending on the nature of the carrier capture process. In our simulation, we tested the correlation between σ and temperature, which included treating σ as temperature-independent, applying an exponential temperature function, and using a ratio of the current temperature to a reference temperature, raised to a power "n." These approaches aim to accurately model the relationship between σ and temperature in the hyperdoped region.

For μ in the substrate region, the established literature reveals well-defined trends in how μ of the Si substrate varies with temperature.[35] In the substrate region, μ decreases with increasing temperature because of increased carrier scattering with phonons. In the Si substrate, μ remains significantly higher than that in the hyperdoped region. However, employing a standard range of values with a temperature dependence of the form $\mu_0\left(\frac{T}{300K}\right)^{-n}$ where n ranges from 0.5 to 3 proves inadequate in capturing the observed dynamics.[35] To address this limitation, we used the same μ_0 value for the hyperdoped region. This approach yielded a more accurate representation of the experimental decay dynamics. Finally, for τ in the substrate region, since the Te dopant concentration is zero, in our simulation, $\tau = \infty$ and no carrier recombination occurs in the substrate region.

In this simulation, we used the forward time-centered space (FTCS) method. This finite-difference technique was instrumental in discretizing the diffusion equation, allowing us to conduct a comprehensive numerical simulation. By combining our assumptions with the diffusion equation and using the FTCS method, we were able to understand how carrier dynamics change with varying temperatures and dopant concentrations in Si:Te.

To best capture the decay dynamics across concentration and temperature, our simulation reveals that μ in the hyperdoped region remains constant at 20 $\text{cm}^2\ (\text{V s})^{-1}$, independent of temperature and concentration. In the substrate region, it is modeled as $\mu = 20\left(\frac{T}{300K}\right)^{-2.5}\ \text{cm}^2\ (\text{V s})^{-1}$. In the hyperdoped region σ follows the relationship $\sigma(T) = \sigma_0\left(\frac{T}{300\ \text{K}}\right)^{-0.5}$, where $\sigma_0 = 2.993 \times 10^{-16}\ \text{cm}^2$. A constant dopant distribution in the hyperdoped region was adopted directly from literature. By selecting these parameters, our simulation was able to accurately replicate the dynamics of Si:Te across varying concentrations and temperatures, aligning closely with the experimental results.

3. Results and Discussion

3.1. Room Temperature THz Conductivity

The carrier recombination dynamics for all samples at room temperature are shown in **Figure 1**. The THz pulses probe conductivity of the material, and the change in the THz transmission

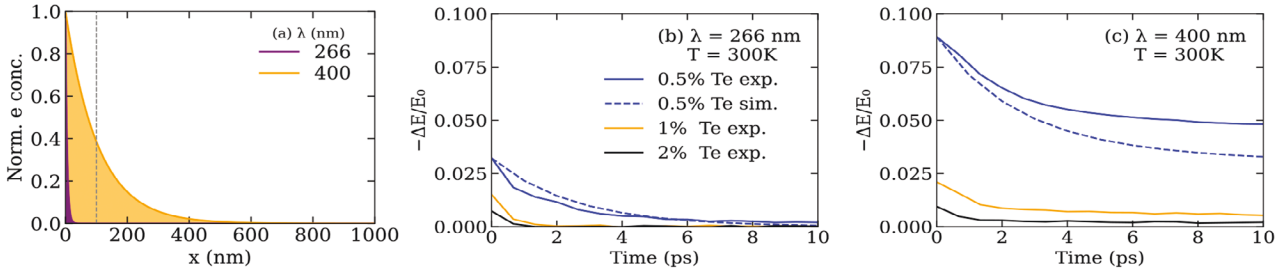

Figure 1. a) Distribution of carriers when excited with 266 and 400 nm light. b,c) THz decay dynamics at room temperature after 266- and 400-nm photoexcitation, respectively. The dashed lines represent the simulated dynamics of the 0.5% Si:Te sample.

amplitude ΔE is proportional to the photoexcited carrier density. Figure 1a presents the normalized depth distribution of the photoexcited carriers in Si:Te when illuminated with two wavelengths, 266 and 400 nm. With 266-nm photoexcitation, carriers are generated within a shallow 5-nm layer at the surface. Conversely, 400-nm photoexcitation results in carriers generated beyond the hyperdoped region, as indicated by the dashed line. Figure 1b shows the decay dynamics of carriers at room temperature after photoexcitation at 266 nm. Figure 1c, in comparison, presents the decay dynamics for a 400 nm excitation, where the decay rate is observed to be relatively slower. The decay dynamics for undoped Si under 266 and 400 nm photoexcitation are shown in Figure S1 (Supporting Information).

The peak of the transient photoconductivity $(-\Delta E/E_0)$ and decay dynamics are strongly correlated with the dopant concentration (Figure 1b,c). As the concentration of dopants increases, the peak value of $(-\Delta E/E_0)$ not only decreases but also exhibits a faster rate of decay. For carrier decay dynamics, an increase in the dopant concentration introduces more recombination sites, which accelerates the carrier recombination process. For dopant concentration dependent $(-\Delta E/E_0)$ we examine the relation between THz transmission and conductivity in detail next.

In this section, we show that the y-axis is relates to both the photoexcited carriers and the background conductivity. The y-axis, $(-\Delta E/E_0)$, in Figure 1b,c is proportional to the photoexcited carrier density, where E_0 is the THz transmission through an unexcited sample and $\Delta E(t)$ is the change in THz transmission after excitation. In all cases, $|\Delta E|$ is less than 10% of E_0, so $(-\Delta E/E_0)/(1+\Delta E/E_0) \approx (-\Delta E/E_0)$. In general, THz waves interact with conductive charge carriers, so in our experiment, both free carriers in equilibrium and free carriers generated by photoexcitation interact with the THz probe beam. Namely, $s_{total} = s_{equilibrium} + s_{photo}$, where $s_{equilibrium}$ represented the background conductivity and s_{photo} represents the contribution from photoexcitation. If the $s_{equilibrium}$ is negligible, the exact relationship between ΔE and conductivity is $(-\Delta E/E_0) = \frac{Z_0 d}{(1+N_{Si})} \times s_{photo}$, where $s_{photo} = \Delta n q \mu$, with q denotes the charge of carriers, and Δn represents the excited carrier concentration. The material constants are $N_{Si} = 3.41$ as the index of refraction of Si in the THz region, $z_0 = 377\Omega$ is the characteristic impedance of free space, d is the optical absorption depth.[42] When $s_{equilibrium}$ is not negligible, then $(-\Delta E/E_0) = \Delta n/(n_0 + A)$, where n_0 is the equilibrium carrier concentration and the material constants are $A = (1+n_{Si})/(z_0 dq\mu)$.[42] Te is an n-type dopant; therefore, with increasing Te concentration, n_0 increases which leads to a reduced $(-\Delta E/E_0)$. Increasing n_0 from the 0.5% Te to 2% Te is the reason for the observed reduction in the peak $(-\Delta E/E_0)$ value at $t = 0$. This analysis provides two key insights: first, $|\Delta E| \propto \Delta n$; second, $|\Delta E|$ diminishes as n_0 increases. For convenience, we denote $(-\Delta E/E_0)$ as s throughout our discussion.

Figure 1c shows a trend similar to Figure 1b regarding the peak s and decay dynamics. However, it also exhibited a slower decay rate than that shown in Figure 1b. As shown in Figure 1a, 400-nm photoexcitation induces carrier generation deep in the substrate region, with far fewer carrier trapping sites than in the hyperdoped region. Additionally, a fraction of carriers generated in the hyperdoped region diffuses into the substrate region, resulting in an overall slower decay relative to the 266-nm photoexcitation. Our simulation, shown by the dashed lines in Figure 1b,c, captures the dopant concentration- and excitation-wavelength-dependent recombination dynamics observed in our experiment.

3.2. Temperature and Depth Dependent Mobility

Figure 2 shows the relationship between the peak s and temperature following photoexcitation at wavelengths of 266 nm and 400 nm. As mentioned previously, as the dopant concentration increases, s decreases because of the increased background conductivity. As a function of temperature, we find that the peak s after 266-nm photoexcitation is constant across the range of temperatures probed. In contrast, Figure 2b displays a clear trend of temperature-dependent peak s after 400-nm photoexcitation.

The temperature-independent peak s observed in Figure 2a supports that μ in the hyperdoped region is temperature independent, as reported in ref. [16]. As mentioned before, $s = \Delta n/(n_0 + A)$, and when examining the peak s before any carrier recombination, Δn is a constant value related only to the photoexcitation fluence. The background carrier density (n_0) is reported to be independent of temperature at dopant concentrations very close to or above the insulator-to-metal transition.[16] Therefore, the temperature-independent peak s suggests that A is also temperature independent, and $A = (1+n_{Si})/(z_0 dq\mu)$. Therefore, our result supports that μ is independent of temperature in the hyperdoped region for all samples, validating the assumption we used in the simulation.

For 400-nm photoexcitation, the peak s decreases with increasing temperature (Figure 2b). At this wavelength, the absorption depth is larger than the thickness of the hyperdoped region (Figure 1a). A portion of the excited carriers is generated in

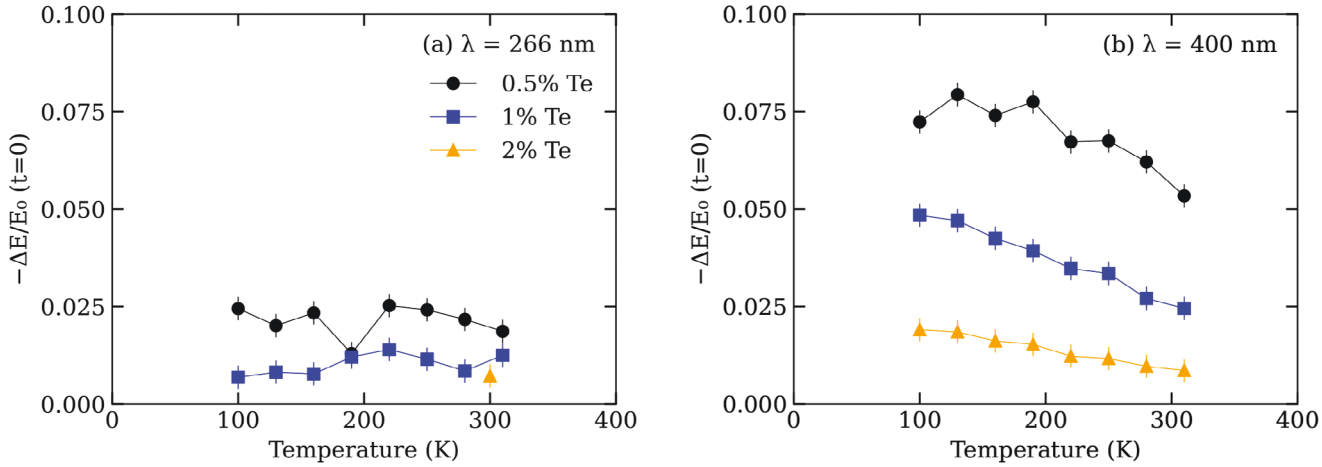

Figure 2. Temperature dependence of the peak transient conductivity. a) When excited at 266 nm, the peak transient conductivity exhibits no temperature dependence, indicating constant mobility in the hyperdoped region. b) In contrast, when excited at 400 nm, the peaks display a clear temperature dependence, which can be attributed to the temperature-dependent mobility in the substrate region.

the substrate region. In the hyperdoped region, μ is temperature independent, but in the substrate region, μ decreases as the temperature increases because of increased phonon scattering. This temperature-dependent mobility in the substrate region affects peak *s*, causing it to decrease with increasing temperature. In summary, by probing the peak *s* as a function of temperature at the two excitation wavelengths, our data support that μ in the hyperdoped region is temperature independent, and μ in the substrate region increases with decreasing temperature.

3.3. Temperature Dependence of Carrier Dynamics

Figure 3 shows temperature-dependent normalized transient *s* to reveal decay trends for 266 and 400-nm photoexcitation. For both photoexcitation wavelengths, the decay rate increases with increasing dopant concentration due to the increased number of recombination centers. In Figures 3a and b, for 266-nm photoexcitation, the decay curve does not show any temperature dependence. Due to the low signal from the highly doped samples (Figure 2a), the noise appeared to be larger in the normalized curves shown in Figure 3. The carrier decays quickly, within 10 ps for the 0.5% sample and within 3 ps for the 1% sample with THz conductivity data showing noise oscillating above and below the baseline after 3ps. For the 2% sample, we only report the room temperature in Figure 3c because the data taken in the temperature-dependent measurement had a low signal with high noise. Based on the temperature-independent behavior of the 0.5

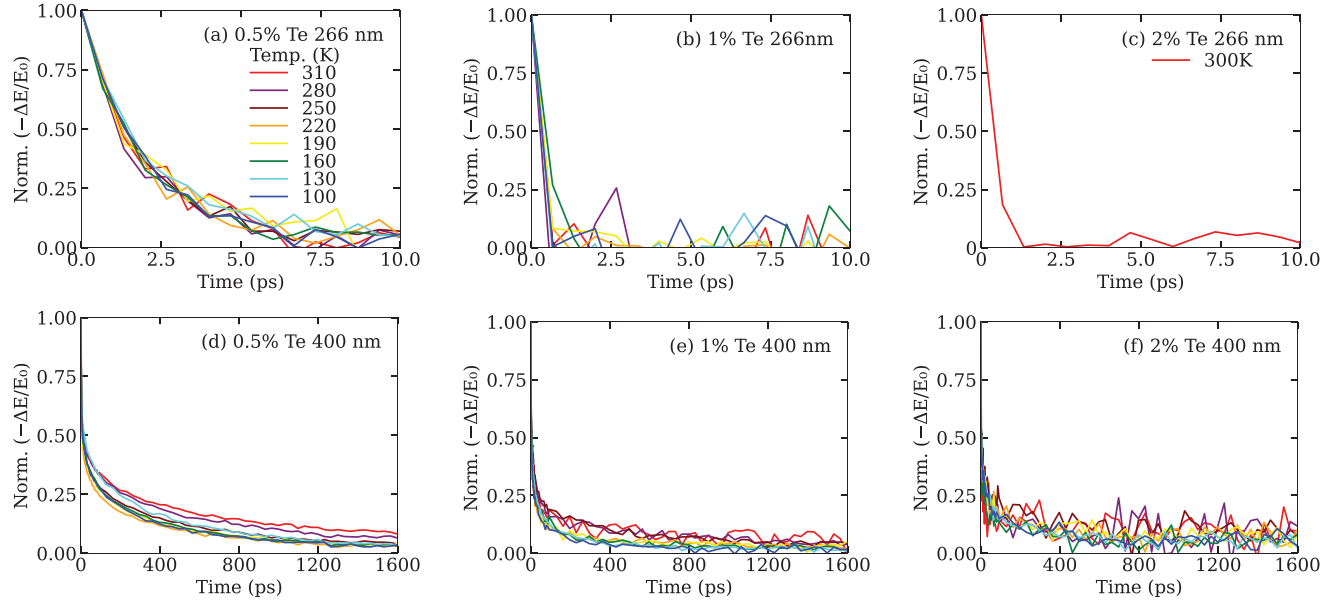

Figure 3. Normalized THz transient conductivity decay dynamics at temperatures ranging from 100 to 310 K for 0.5, 1, and 2% Si:Te after 266-nm photoexcitation a–c) and 400-nm photoexcitation d–f)).

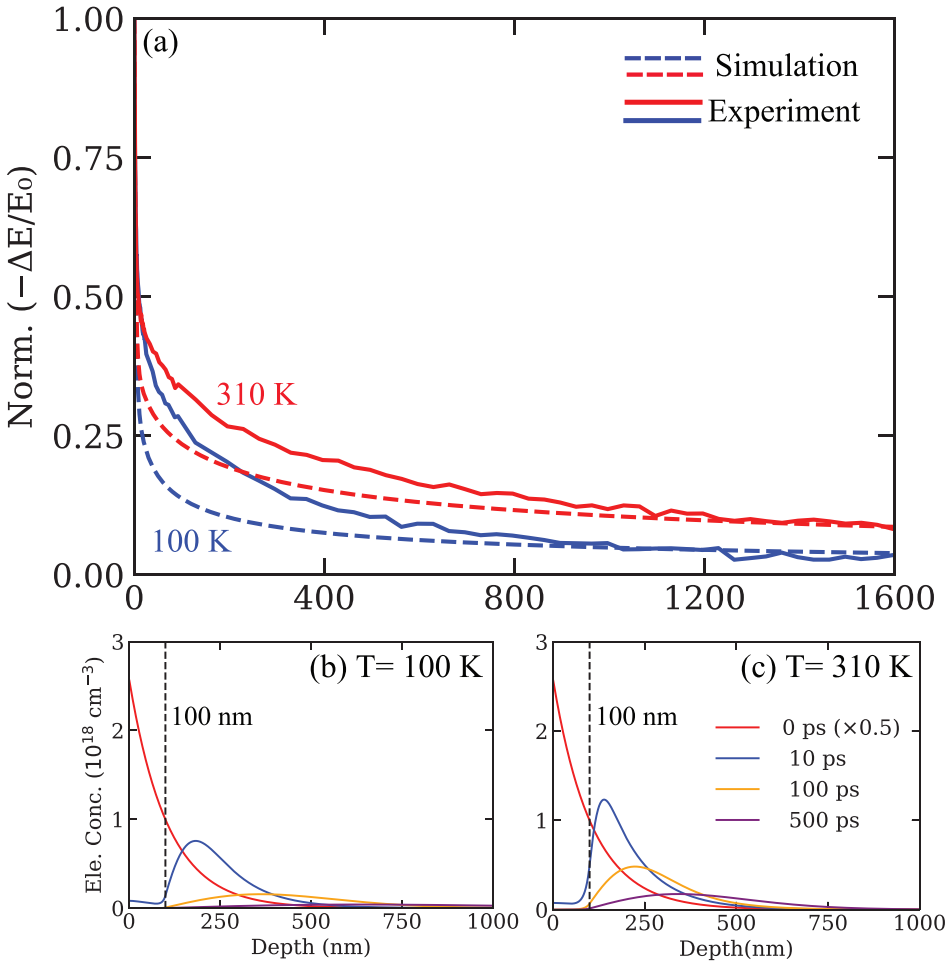

Figure 4. Comparison of experimental and simulated decay dynamics after 400-nm photoexcitation for 0.5% Si:Te at temperatures of 100 and 300K a). Simulated carrier distribution profiles at selective times after photoexcitation at 100 K b) and 300 K c).

and 1% sample, we assume the 2% sample will be similar. In contrast, at 400-nm photoexcitation there is a temperature dependence in the transient *s* (Figure 3d–f). This shows that the decay rate decreases with increasing temperature. This temperature-dependent trend is particularly pronounced for the 0.5% sample and becomes less distinct with increasing dopant concentration.

Figure 4 shows the experimental and simulated decay dynamics along with the simulated carrier distribution profile for 400-nm photoexcitation. Figure 4a presents the experimental and simulated normalized transient *s* for the 0.5% Te sample at 100 and 310 K. Figure 4b,c shows simulated carrier distribution snapshots at different times at two different temperatures, 100 and 310 K, respectively. Qualitatively, the simulated decay dynamics match the experimental curves at the two different temperatures. This indicates that the simulation successfully captures the experimental trends, which validates our model to explain the influence of temperature on the carrier lifetime.

The carrier distribution profiles shown in Figure 4b,c indicate that a significant number of carriers diffuse away to the substrate region following the initial excitation, a process driven by the concentration gradient. Given the high recombination rate of the hyperdoped region, the electron density within this region ($x < 100$ nm) becomes significantly reduced. As a result, carriers that have initially diffused away are subsequently drawn back into the hyperdoped region, where they are more likely to recombine. At 100 K, carriers diffuse further away from the hyperdoped region compared to those at 310 K. This is because of the higher μ value in the substrate region at lower temperatures. As a result, not only do carriers diffuse further away, they also back diffuse into the hyperdoped region faster, leading to the faster decay observed at lower temperatures when excited at 400 nm.

3.4. Discussion

To show that our simulation works for all dopant concentrations, temperatures, and photoexcitation wavelengths, **Figure 5** shows a comparison of the experimental and simulated normalized decays across all the samples at 100 and 310 K. Figure 5a–c shows simulated dynamics compared with experimental data across the concentration for 266-nm photoexcitation. Figure 5d–f and Figure S2 (Supporting Information) present analogous data for 400-nm photoexcitation. The agreement between the experimental data and simulation shows that we successfully found one set

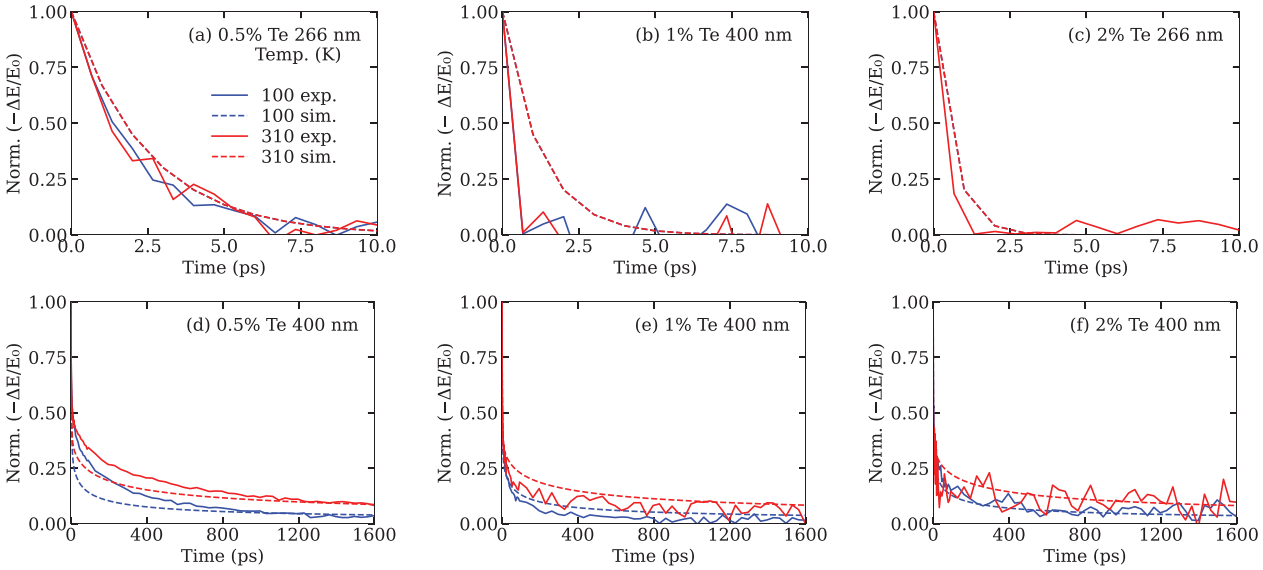

Figure 5. Comparison of normalized experimental and simulated decay dynamics for Si:Te at various concentrations and temperatures (100 and 310 K) after 400- and 266-nm photoexcitation.

of parameters: $\sigma(T)$, $\mu_{Si}(T)$, and μ_{HD}, to produce simulation curves that simultaneously match the experimental data at different excitation wavelengths, temperatures, and dopant concentrations.

While our simulation model effectively captures the general trends and mechanisms observed in the experimental data, some discrepancies remain. These discrepancies arise from specific assumptions and simplifications such as uniform distribution of dopants and constant mobility within the hyperdoped region, which do not fully capture the complexities of the actual material. Additionally, factors such as surface defects and the presence of a p-n junction are not accounted for in the current model. Despite these limitations, the strength of our model lies in its simplicity and ability to describe the overall behavior of the system under various conditions.

Through this simulation, we revealed that the carrier lifetime in Si:Te is independent of temperature. Figure 5a–c shows constant decay dynamics across the temperature range, and the temperature dependence shown in Figure 5d,e is driven by carrier diffusion alone. The recombination rate in this region can be described by Equation (1). As temperature increases, σ decreases proportionally to $1/\sqrt{T}$, while the v_{thermal} increases proportionally to $\sqrt{T}$. This inverse relationship results in their temperature effects canceling each other, leading to a constant recombination rate in the hyperdoped region across all temperatures.

Wang *et al.* demonstrated that the responsivity of Si:Te photodiodes to sub-bandgap light increases at lower temperatures.[11,12] In our study, we aimed to determine whether this increased responsivity at lower temperatures is linked to carrier lifetimes in the hyperdoped region. In Refs. [11, 12], measurements in the photovoltaic mode (without bias) showed that the responsivity extended from wavelengths of 4 to 5 μm as the temperature decreased from 300 to 20 K. This enhancement was attributed to the reduced thermal generation of carriers from the intermediate band to the conduction band, which increases the optical responsivity at lower temperatures. Our study indicates that the carrier lifetimes in the hyperdoped region remain constant across varying temperatures, so other mechanisms, such as the reduction of thermal generation of carriers, could indeed be the reason for the improved sub-bandgap light sensing at lower temperatures.

Lastly, an increase in the dopant concentration leads to more recombination sites, resulting in an increased recombination rate and a decreased carrier lifetime. Our finding in Si:Te is consistent with literature reports on lighter chalcogen dopants, which showed a reduced carrier lifetime with increasing dopant concentration for Si:S,[42,43] and for Si:Se.[42] In ref. [43], the authors showed that carrier lifetime improvement was achieved by the removal of dopants, but it also led to a significant reduction in the absorption of sub-bandgap light. Similar lifetime modifications by dopant profile engineering have been reported in gold-hyperdoped Si.[15] It is therefore unsurprising that the demonstrated Si:Te photodiode with extended infrared sensing was achieved using the lowest dopant concentration among the set of samples studied.[11,12] Similar to sub-bandgap excitation, 266-nm photoexcitation in our study has all carriers generated and confined in the hyperdoped region, so our findings are particularly relevant to sub-bandgap photosensing in Si:Te.

4. Conclusion

We studied the influence of variations in temperature and dopant concentration on the charge-carrier dynamics of Si:Te. For photoexcitation at 266 nm, the peak *s* remains unaffected by temperature. This is attributed to the constant mobility within the hyperdoped region, irrespective of both the temperature and Te concentration, and the confinement of the excited carriers in this region. Our simulation revealed that the counterbalancing effects of temperature on the capture cross-section and thermal velocity result in a temperature-independent recombination rate, ensuring that the carrier lifetime remains constant despite the temperature change. In contrast, for 400-nm photoexcitation, the

peak *s* decreases with increasing temperature due to carriers generated in the substrate region having reduced mobility. The reduction in *s* decay rate at this wavelength, as the temperature rises, is explained in the simulation by the relationship between carrier diffusion and temperature-dependent mobility. For both photoexcitation wavelengths, the carrier lifetime decreases with increasing concentration because of the increased number of recombination sites. The observed carrier dynamics in Si:Te under different temperatures, photoexcitation conditions, and dopant concentrations offer crucial insights into the unique properties of hyperdoped Si.

5. Experimental Section

P-type Si substrates with resistivities of 1 −10 Ω cm were used to fabricate Si:Te. A two-step ion implantation was used for hyperdoping to achieve a uniform dopant profile. The initial ion implantation was conducted at 150 keV with doses of 6.2×10^{14}, 3.1×10^{15}, and 6.2×10^{15} cm^{-2}. This was followed by a second implantation at 50 keV with doses of 1.6×10^{14}, 1.2×10^{15}, and 2.5×10^{15} cm^{-2} to achieve Te concentrations of 0.5, 1, and 2 atomic%, respectively. The PLM process was carried out using an XeCl excimer laser operating at 308 nm with a pulse duration of 28 ns and a fluence of 1.2 Jcm^{-2}. More detailed information on sample fabrication can be found in Ref. [12].

TRTS was used to conduct temperature-dependent non-contact photoconductivity decay measurements. The experiment used a Ti:Sapphire laser amplifier to produce 800 nm light pulses, each with 2 mJ energy, at a 1 kHz repetition rate, and the laser beam was split into three paths. The first path generated coherent and short THz pulses through the two-color air-plasma method.[44] The THz radiation was used for probing the photoconductivity of the Si:Te sample. The second path was dedicated to THz detection using a 1-mm ZnTe crystal.[45,46] The electro-optical properties of the ZnTe crystal changed the polarization of the 800 nm light in the second beam path in the presence of the coherent and short THz, allowing one to detect THz amplitude with sub-picosecond time resolutions.[47]

The third path of the fs-laser was frequency converted for photoexcitation of the samples. To achieve 400- nm photoexcitation, the 800-nm beam passes through a beta-barium borate (BBO) crystal for second harmonic generation (SHG) and effectively doubling the frequency of the light and halving its wavelength to 400 nm. The 266 nm optical pump was generated through a frequency-tripling process involving two stages. After the aforementioned SHG process, both the original 800 nm and the newly created 400 nm beams were directed into another BBO crystal (the THG crystal) for sum-frequency mixing. A delay compensator and a dual waveplate were placed before the THG crystal for fine-tuning the timing and polarization of the 800 and 400-nm beams and hence enhancing the efficiency of sum-frequency mixing. This process lead to the generation of a beam with one-third of the original wavelength, 266 nm.

Photoexcited carriers in Si:Te interact with the THz probe pulse, leading to the attenuation of the THz signal. The pump power was 1 mW. The spot size for 400 nm light is 0.0374 cm^2 and for 266 nm light is 0.027 cm^2. The time delay between the pump pulse and the probe pulse was controlled by a 300-mm delay stage, yielding an observation window of 2 ns. This change in THz transmission represents transient photoconductivity.

In this study, the Si:Te sample was placed in a cryostat and cooled down to 100 K using liquid nitrogen. This kept the sample at a stable, low temperature, allowing us to increase the temperature using a resistive heater in controlled steps of 30 K. Transient photoconductivity measurements began at 100 K and continued as the temperature was increased to 310 K.

Supporting Information

Supporting Information is available from the Wiley Online Library or from the author.

Acknowledgements

The authors express their gratitude to the Ion Beam Center (IBC) at Helmholtz Zentrum Dresden-Rossendorf (HZDR) for conducting the implantations. M.S.S. acknowledges the financial support received from the Deutsche Forschungsgemeinschaft under grant No. WA4804/1-1 (445049905). M.-J.S. and K.M.A. Rahman were supported by NSF DMR-2316827.

Conflict of Interest

The authors declare no conflict of interest.

Data Availability Statement

The data that support the findings of this study are available from the corresponding author upon reasonable request.

Keywords

hyperdoping, photoconductivity, time-resolved THz spectroscopy (TRTS), transient conductivity

Received: May 22, 2024
Revised: August 27, 2024
Published online:

[1] S. H. Pan, D. Recht, S. Charnvanichborikarn, J. S. Williams, M. J. Aziz, *Appl. Phys. Lett.* **2011**, *98*, 121913.
[2] W. Yang, A. J. Akey, L. Smillie, J. P. Mailoa, B. Johnson, J. McCallum, D. Macdonald, T. Buonassisi, M. J. Aziz, J. Williams, *Phys. Rev. Mater.* **2017**, *1*, 074602.
[3] B. Franta, M.-J. Sher, Y.-T. Lin, K. C. Phillips, E. Mazur, in *Laser Appl. Microelectron. Optoelectron. Manufact. (LAMOM) XVII*, vol. *8243*, SPIE, Washington USA **2012**, pp. 321–327.
[4] J. M. Warrender, *Appl. Phys. Rev.* **2016**, *3*, 031104.
[5] S. Q. Lim, J. S. Williams, *Micro* **2021**, *2*, 1.
[6] W. Yang, J. Mathews, J. Williams, *Mater. Sci. Semicond. Process.* **2017**, *62*, 103.
[7] E. García-Hemme, D. Caudevilla, S. Algaidy, F. Pérez-Zenteno, R. García-Hernansanz, J. Olea, D. Pastor, A. del Prado, E. San Andres, I. Martil, G. González-Díaz, *Adv. Electron. Mater.* **2022**, *8*, 2100788.
[8] T. Gimpel, S. Winter, M. Boßmeyer, W. Schade, *Sol. Energy Mater. Sol. Cells* **2018**, *180*, 168.
[9] C. Li, J.-H. Zhao, Z.-G. Chen, *J. Alloys Compd.* **2021**, *883*, 160765.
[10] J. P. Mailoa, A. J. Akey, C. B. Simmons, D. Hutchinson, J. Mathews, J. T. Sullivan, D. Recht, M. T. Winkler, J. S. Williams, J. M. Warrender, P. D. Persans, M. J. Aziz, T. Buonassisi, *Nat. Commun.* **2014**, *5*, 3011.
[11] M. Wang, E. García-Hemme, Y. Berencen, R. Hübner, Y. Xie, L. Rebohle, C. Xu, H. Schneider, M. Helm, S. Zhou, *Adv. Opt. Mater.* **2021**, *9*, 2001546.
[12] M. Wang, Y. Berencén, E. García-Hemme, S. Prucnal, R. Hübner, Y. Yuan, C. Xu, L. Rebohle, R. Böttger, R. Heller, H. Schneider, W. Skorupa, M. Helm, S. Zhou, *Phys. Rev. Appl.* **2018**, *10*, 024054.
[13] H. Jiang, M. Wang, J. Fu, Z. Li, M. S. Shaikh, Y. Li, C. Nie, F. Sun, L. Tang, J. Yang, T. Qin, D. Zhou, J. Shen, J. Sun, S. Feng, M. Zhu, U. Kentsch, S. Zhou, H. Shi, X. Wei, *ACS Nano* **2022**, *16*, 12777.
[14] M. T. Winkler, D. Recht, M.-J. Sher, A. J. Said, E. Mazur, M. J. Aziz, *Phys. Rev. Lett.* **2011**, *106*, 178701.
[15] S. S. Dissanayake, N. O. Pallat, P. K. Chow, S. Q. Lim, Y. Liu, Q. Yue, R. Fiutak, J. Mathews, J. S. Williams, J. M. Warrender, M.-L. Sher, *APL Mater.* **2022**, *10*, 111106.

[16] M. Wang, A. Debernardi, W. Zhang, C. Xu, Y. Yuan, Y. Xie, Y. Berencén, S. Prucnal, M. Helm, S. Zhou, *Phys. Rev. B* **2020**, *102*, 085204.
[17] B. P. Bob, A. Kohno, S. Charnvanichborikarn, J. M. Warrender, I. Umezu, M. Tabbal, J. S. Williams, M. J. Aziz, *J. Appl. Phys.* **2010**, *107*, 123506.
[18] I. Umezu, J. M. Warrender, S. Charnvanichborikarn, A. Kohno, J. S. Williams, M. Tabbal, D. G. Papazoglou, X.-C. Zhang, M. J. Aziz, *J. Appl. Phys.* **2013**, *113*, 213501.
[19] M.-J. Sher, Y.-T. Lin, M. T. Winkler, E. Mazur, C. Pruner, A. Asenbaum, *J. Appl. Phys.* **2013**, *113*, 063520.
[20] J. Sullivan, C. Simmons, J. Krich, A. Akey, D. Recht, M. J. Aziz, T. Buonassisi, *J. Appl. Phys.* **2013**, *114*, 103701.
[21] M.-J. Sher, E. G. Hemme, *Semicond. Sci. Technol.* **2023**, *38*, 033001.
[22] J. J. Krich, B. I. Halperin, A. Aspuru-Guzik, *J. Appl. Phys.* **2012**, *112*, 13707.
[23] J. T. Sullivan, C. B. Simmons, T. Buonassisi, J. J. Krich, *IEEE J. Photovoltaics* **2014**, *5*, 212.
[24] M. Wang, R. Hübner, C. Xu, Y. Xie, Y. Berencén, R. Heller, L. Rebohle, M. Helm, S. Prucnal, S. Zhou, *Phys. Rev. Mater.* **2019**, *3*, 044606.
[25] D. Recht, J. T. Sullivan, R. Reedy, T. Buonassisi, M. J. Aziz, *Appl. Phys. Lett.* **2012**, *100*, 112112.
[26] C. B. Simmons, A. J. Akey, J. P. Mailoa, D. Recht, M. J. Aziz, T. Buonassisi, *Adv. Funct. Mater.* **2014**, *24*, 2852.
[27] Z. Yu, J. Cong, A. Khan, P. Hang, D. Yang, X. Yu, *Nanotechnology* **2023**, *35*, 115703.
[28] H. Wen, J. He, J. Hong, S. Jin, Z. Xu, H. Zhu, J. Liu, G. Sha, F. Yue, Y. Dan, *Adv. Opt. Mater.* **2020**, *8*, 2000720.
[29] B. R. Tull, M. T. Winkler, E. Mazur, *Appl. Phys. A* **2009**, *96*, 327.
[30] C. Simmons, A. J. Akey, J. J. Krich, J. T. Sullivan, D. Recht, M. J. Aziz, T. Buonassisi, *J. Appl. Phys.* **2013**, *114*, 243514.
[31] R. Schaub, G. Pensl, M. Schulz, C. Holm, *Appl. Phys. A* **1984**, *34*, 215.
[32] H. Grimmeiss, E. Janzen, H. Ennen, O. Schirmer, J. Schneider, R. Wörner, C. Holm, E. Sirtl, P. Wagner, *Phys. Rev. B* **1981**, *24*, 4571.
[33] D. M. Caughey, R. Thomas, *Proc. IEEE* **1967**, *55*, 2192.
[34] S. Qin, S. A. Prussin, J. Reyes, Y. J. Hu, A. McTeer, *IEEE Trans. Plasma Sci.* **2010**, *39*, 587.
[35] R. F. Pierret, G. W. Neudeck, *Advanced semiconductor fundamentals*, vol. *6*, Addison-Wesley Reading, MA, **1987**.
[36] A. Schenk, *Solid-State Electron.* **1992**, *35*, 1585.
[37] C. Henry, D. V. Lang, *Phys. Rev. B* **1977**, *15*, 989.
[38] M. Ichimura, H. Tajiri, T. Ito, E. Arai, *J. Electrochem. Soc.* **1998**, *145*, 3265.
[39] B. B. Paudyal, K. R. McIntosh, D. H. Macdonald, G. Coletti, *J. Appl. Phys.* **2010**, *107*, 1588.
[40] S. Rein, *Lifetime spectroscopy: A Method of Defect Characterization in Silicon for Photovoltaic Applications*, vol. *85*, Springer Science & Business Media, Heidelberg, Germany **2005**.
[41] R. Ulbricht, E. Hendry, J. Shan, T. F. Heinz, M. Bonn, *Rev. Mod. Phys.* **2011**, *83*, 543.
[42] M.-J. Sher, C. B. Simmons, J. J. Krich, A. J. Akey, M. T. Winkler, D. Recht, T. Buonassisi, M. J. Aziz, A. M. Lindenberg, *Appl. Phys. Lett.* **2014**, *105*, 053905.
[43] S. Schäfer, X. Liu, P. Mc Kearney, S. Paulus, B. Radfar, V. Vähänissi, H. Savin, S. Kontermann, *Phys. Status Solidi A* **2024**, https://doi.org/10.1002/pssa.202400132.
[44] H. Roskos, M. Thomson, M. Kreß, T. Löffler, *Laser Photonics Rev.* **2007**, *1*, 349.
[45] F. A. Hegmann, O. Ostroverkhova, D. G. Cooke, Photophysics of Molecular Materials: From Single Molecules to Single Crystals (Eds: H. Bässler, A. Köhler), Wiley Online Library, **2005**, pp. 367–428, https://doi.org/10.1002/3527607323.
[46] H. Wen, A. M. Lindenberg, *Phys. Rev. Lett.* **2009**, *103*, 023902.
[47] S. S. Dissanayake, N. Ferdous, H. H. Gandhi, D. Pastor, T. T. Tran, J. S. Williams, M. J. Aziz, E. Mazur, E. Ertekin, M.-J. Sher, *Phys. Rev. Appl.* **2021**, *15*, 064058.